HHS Public Access

Author manuscript

Nat Microbiol. Author manuscript; available in PMC 2020 January 22.

Published in final edited form as:

Nat Microbiol. 2019 November ; 4(11): 1951–1963. doi:10.1038/s41564-019-0504-8.

The secreted kinase ROP17 promotes *Toxoplasma gondii* dissemination by hijacking monocyte tissue migration

Lisa L Drewry[1], **Nathaniel G Jones**[1,2], **Quiling Wang**[1], **Michael D Onken**[3], **Mark J Miller**[4], **L David Sibley**[*,1]

[1.] Department of Molecular Microbiology, Washington University School of Medicine, St. Louis MO 63110

[2.] Current address: York Biomedical Research Institute, Department of Biology, University of York, Wentworth Way, Heslington, York YO10, U.K.

[3.] Department of Biochemistry and Molecular Biophysics, Washington University School of Medicine, St. Louis, MO 63110

[4.] Department of Medicine, Division of Infectious Diseases, Washington University School of Medicine, St. Louis MO 63110

Abstract

The protozoan parasite *Toxoplasma gondii* is thought to exploit monocyte trafficking to facilitate dissemination across endothelial barriers such as the blood-brain barrier. Here we analyzed the migration of parasitized monocytes in model endothelial and interstitial environments. We report that infection enhanced monocyte locomotion on the surface of endothelial cells, but profoundly inhibited monocyte transmigration across endothelial barriers. In contrast, infection robustly increased monocyte and macrophage migration through collagen-rich tissues in a Rho/ROCK-dependent manner consistent with integrin-independent interstitial migration. We further demonstrated that the secreted *T. gondii* protein kinase ROP17 was required for enhanced tissue migration. *In vivo*, ROP17-deficient parasites failed to upregulate monocyte tissue migration and exhibited an early dissemination delay, leading to prolonged mouse survival. Our findings indicate that the parasite-induced changes in monocyte motility likely facilitate the transport of *T. gondii*

[*]Corresponding author.

AUTHOR CONTRIBUTIONS

L.L.D. and L.D.S. designed experiments and wrote the manuscript. N.G.J. generated *T. gondii* strains used for time lapse microscopy. Q.W. collaborated on design and execution of animal studies. M.D.O. collaborated on design and interpretation of Rho GTPase inhibitor studies. L.L.D. and M.J.M. designed and performed 2-photon imaging experiments. L.L.D. performed all other experiments and analyzed data. L.D.S. supervised the study. All authors critically reviewed and approved the manuscript.

COMPETING INTERESTS

The authors declare no competing financial interests.

DATA AVAILABILITY

All data generated and analyzed during this study are included within the manuscript and associated Supplementary Information.

SUPPLEMENTARY INFORMATION

Supplementary Information: Supplementary Figures 1–6, Supplementary Methods, Supplementary Table 1 (*T. gondii* strains), Supplementary Table 2 (plasmids), Supplementary Table 3 (oligonucleotides), Supplementary References, Supplementary Video Legends Supplementary Videos 1–6: Six time-lapse microscopy videos of monocyte locomotion corresponding to the data shown in Fig 2 and Fig 6 are included.

through tissues and promote systemic dissemination, rather than shuttle parasites across the blood-brain barrier via extravasation.

MAIN

The protozoan parasite *Toxoplasma gondii* causes severe disease in immunocompromised humans[1] and is among the few pathogens that invades the central nervous system (CNS) by crossing the blood-brain barrier (BBB). *T. gondii* is theorized to hijack leukocytes as shuttles that enable extravasation across the BBB[2,3]. Infected leukocytes could also aid dissemination at several other infection stages. After oral ingestion, parasites traverse intestinal epithelium and enter the lamina propria[4,5], thus immediately encountering resident phagocytes[3,6,7] and later recruited inflammatory monocytes[8]. From this infection nidus, parasites disseminate to draining lymph nodes, the blood, spleen, and eventually, all organs including the brain[4,5,9]. Infected leukocytes could promote dissemination by carrying parasites out of the lamina propria, through the lymphatic vasculature and into the circulation. Circulating leukocytes could also deliver parasites across endothelial barriers and into new tissues via extravasation, a sequential process that is initiated by selectin-mediated leukocyte capture, progresses to integrin-based adhesion and vascular crawling, and commences with endothelial traversal[10].

As one of the most severe complications of toxoplasmosis is encephalitis[1], the potential for extravasating leukocytes to ferry parasites across the BBB has been keenly investigated[9,11]. *In vitro* modelling of this process revealed that parasite infection enhanced primary human monocyte crawling on human umbilical vein endothelial cells (HUVEC) without significantly altering transendothelial migration (TEM)[12,13]. These findings prompted a proposal that infected monocytes are poised to deliver parasites across the BBB[3,14]. However, infection diminished integrin-mediated endothelial adherence[15,16], a step generally considered prerequisite to endothelial crawling and transmigration[10]. Numerous reports have showed that *T. gondii*-infected dendritic cells (DCs) exhibit hypermigratory behavior[17–20]. However, during murine infection nearly all parasitized leukocytes in the blood are $CD11b^+$ monocytes[11]. Consistent with a role for monocytes in dissemination, adoptive transfer of infected monocytes hastens dissemination to the CNS in mice[11]. However, a different conclusion was reached by a recent study assessing the potential for blood-localized extracellular parasites to invade the mouse CNS, which noted that adoptively transferred infected monocytes were readily detected in brain vasculature but not the parenchyma[9]. In total, current data is inconsistent with a simple model where infected monocytes are the primary vehicle for parasites to cross the BBB.

Here we examine how infected monocytes migrate using *in vitro* models that mimic vascular *vs.* tissue environments. We found that infection inhibited transmigration across the BBB and peripheral endothelium, processes that require integrin-dependent adhesion. In contrast, infection enhanced monocyte and macrophage migration through collagen-rich tissues, distinct environments that support integrin-independent motility. The tissue migration of parasitized monocytes and macrophages required host Rho/ROCK signaling, and the secreted parasite kinase ROP17, which was also required for efficient dissemination *in vivo*.

Our findings suggest that in *T. gondii*-infected monocytes, Rho-activation inhibits extravasation and opposes a BBB Trojan horse seeding mechanism, while upregulating interstitial migration to promote the rapid spread of infected cells within tissues and systemic parasite dissemination.

RESULTS

T. gondii infection impaired THP-1 monocyte endothelial adherence and transmigration

We used hCMEC/D3 brain endothelial cells cultured on transwell inserts[21] to model TEM across the BBB. Uninfected THP-1 monocytes exhibited time-dependent TEM across hCMEC/D3 monolayers, and enhanced migration in response to a chemotactic MCP-1 gradient (Fig. 1a). Strikingly, *T. gondii* pre-infection inhibited spontaneous and chemotaxis-driven TEM through hCMEC/D3 monolayers (Fig. 1a). We extended these studies to primary human monocytes and found that TEM was inhibited by prior *T. gondii* infection, at multiple time points (1 *vs* 4 h) and infection densities (MOI 1.5 *vs* 4) (Fig. 1b). We further established that parasite-inhibition of TEM was observed with primary and immortalized endothelial cells derived from multiple tissues, a hCMEC/D3-astrocyte co-culture system that more faithfully models the BBB[21], and parasite strains representing all major North American lineages and a highly genetically divergent South American isolate (Supplementary Fig. 1). Notably, the very low basal migration of THP-1 monocytes through HUVEC (Supplementary Fig. 1) may explain why an earlier study failed to detect parasite-induced inhibition of TEM[12].

We hypothesized that the failure of parasitized monocytes to transmigrate may stem from defects in integrin-mediated adherence and tested this by measuring adherence to hCMEC/D3 monolayers. As expected, pre-activation of hCMEC/D3 with the inflammatory cytokines TNFα and IFNγ enhanced THP-1 monocyte adherence (Fig. 1c). In contrast, infection inhibited adherence to resting and cytokine-activated hCMEC/D3 monolayers (Fig. 1c). We next asked if this inhibition derived from defects in affinity- or avidity-enhancement of integrin-mediated adherence[22]. We used total internal reflection fluorescence (TIRF) microscopy to assess avidity-enhancing integrin mobilization in THP-1 monocytes adhering to fibronectin ligands. TIRF imaging revealed that infected cells fail to spread on fibronectin-coated surfaces (Supplementary Fig. 2), forming significantly smaller surface footprints and fewer detectable foci of the integrins LFA-1 and VLA-4 at or just above the fibronectin-coated surface, *vs* mock-treated controls (Fig. 1d–h). Flow cytometric analysis of suspension THP-1 monocytes established that infection did not alter surface expression of LFA-1 or VLA-4, or $MnCl_2$-induced integrin unfolding into high affinity conformations (Supplementary Fig. 2). Consistent with this finding, the surface integrins of THP-1 monocytes adhering to fibronectin stained positively with an antibody specific to high affinity beta-1 integrin (Supplementary Fig. 2).

Collectively, these results suggest that defects in avidity-enhancing integrin mobilization lead to inefficient adherence of infected monocytes to our model BBB, resulting in subsequent failure to transmigrate through the endothelium.

Parasitized THP-1 monocytes migrated with amoeboid morphology

We next asked whether, despite their defects in integrin-mediated adherence, infected monocytes could effectively crawl on model BBB, as was reported with HUVEC[12]. To analyze migration, we cultured hCMEC/D3 cells on a soft polyacrylamide substrate that enhances endothelial maturation[23], and observed the locomotion of THP-1 monocytes expressing the actin polymerization reporter F-tractin-eGFP by video microscopy[24]. We found that infection enhanced THP-1 monocyte migration velocity and displacement across hCMEC/D3 cells (Fig. 2a). Intriguingly, the morphology of infected THP-1 monocytes migrating on hCMEC/D3 cell monolayers markedly differed from mock-treated cells (Fig. 2b–d, Supplementary Videos 1–3). As expected for cells crawling on endothelium, mock-treated cells moved by forming pointed pseudopodial structures at their leading edge that were enriched in F-actin (Fig. 2b–c, red arrows, Supplementary Video 1). In contrast, infected cells rarely formed pseudopodial extensions, instead moving in an amoeboid manner typified by a rounded and flowing morphology featuring frequent spherical membrane protrusions (Fig. 2b, yellow arrows, Video 2). A pronounced F-actin-rich leading edge was typically absent in migrating infected cells, and their membrane protrusions instead appeared to be stabilized by F-actin recruitment post-formation (Fig. 2b,d, Supplementary Videos 2–3), consistent with the dynamics of bleb-based motility[25]. We quantified the number of structures consistent with pseudopodia (defined by pointed morphology) or blebs (defined by rounded morphology and delayed F-actin recruitment) formed during migration (Fig. 2c–d). Infected cells formed significantly fewer pseudopodia and more blebs than mock-treated controls (Fig. 2c–d).

In summary, although infected THP-1 monocytes migrated efficiently over hCMEC/D3 endothelial cells, their morphology was inconsistent with canonical adhesion-based vascular crawling and instead reminiscent of reports of amoeboid or bleb-driven motility[25,26].

T. gondii infection enhanced monocyte migration through collagen-rich tissues

The amoeboid morphology of migrating parasitized THP-1 monocytes led us to hypothesize that the parasite may be activating a motility mode similar to integrin-independent leukocyte migration through tissue interstitium[26]. We tested this possibility using a simple migration assay[27] where cells migrate through 3-D matrices of polymerized collagen I, the primary component of tissue interstitium[28]. We generated 3-D renderings from Z-stack images of fluorescently-labeled THP-1 monocytes captured after migration into the matrix (Fig. 3a–b, top), and used automated cell identification to quantify the number of monocytes that penetrated into the matrix, and their relative vertical positions (Fig. 3a–b, bottom). Infection increased the number of THP-1 monocytes that penetrated into collagen matrices, and the distance they migrated (Fig. 3a–d). Enhanced migration was observed whether 3-D migration was spontaneous or chemokinetically stimulated with MCP-1 chemokine (Fig. 3c–d). Infection also enhanced the migration of primary human monocytes (Supplementary Fig. 3), confirming the robustness of this phenotype. Because monocytes typically differentiate into phagocytes upon entering tissues, we asked if infection enhanced macrophage migration in this system and again found that infection enhanced migration of RAW 264.7 macrophages and murine bone marrow-derived macrophages (Supplementary Fig. 3).

To better reflect the complex composition and architecture of tissue interstitium, we then adapted a method developed to analyze leukocyte migration through dermal ear sheets[26,29]. We labeled the vessels in the interstitium of *ex vivo* murine ear dermis by laminin staining, and then collected time-lapse microscopy images of RAW 264.7 macrophages crawling within the dermis (Fig. 3e–f). As in the collagen I matrices, infection stimulated migration within ear dermis, significantly increasing both the distanced traveled and velocity of migrating RAW macrophages (Fig. 3g–h). Taken together, our results show that *T. gondii* infection enhances macrophage migration in collagen-rich tissue substrates.

Migration of infected cells relies upon host Rho/ROCK and parasite ROP17

Having determined that *T. gondii*-infected monocytes fail to efficiently traverse endothelial barriers yet robustly migrate through collagen-rich tissues, we next investigated the mechanism by which infection specifically enhances tissue migration.

Monocytes and macrophages can migrate through 3-D substrates via distinct modes that differ in their dependence on integrins: Rho-dependent amoeboid swimming based on actomyosin contractility; and Rac-dependent mesenchymal crawling based on branched actin protrusion[30–32]. We used the compounds ML-141, NSC-23766, and Rhosin to disrupt Cdc42, Rac, and Rho signaling[33] (Fig. 4a), and found that only inhibition of Rho decreased migration of parasitized THP-1 monocytes (Fig. 4b). We further found that inhibition of the Rho effector ROCK with the compound Y-27632 significantly decreased the distance traveled by parasitized THP-1 monocytes (Fig. 4b). In contrast, inhibition of the Rho effector PKC-α with the compound Gö 6976[34] had a minimal effect on migration (Fig. 4b). Rho/ROCK signaling often leads to motility via formin-mediated actin polymerization. Supporting the relevance of Rho and ROCK in our system, we found that SMIFH2 inhibition of formins[35] had a significantly larger dampening effect on the migration of infected THP-1 monocytes than CK-666[36] inhibition of the branched actin nucleator Arp2/3 (Fig. 4b). Migration of infected RAW 264.7 macrophages and murine bone marrow-derived macrophages was also blocked by Y-27632 ROCK inhibition (Supplementary Fig. 3), suggesting a shared mechanism of enhanced migration in human monocytes and murine macrophages.

We next tested whether infection also enhanced mesenchymal migration through Matrigel. Infection did not robustly enhance migration through dense Matrigel (Supplementary Fig. 3). However, a protease inhibitor cocktail that suppresses mesenchymal migration[37] subtly decreased the number of infected macrophages that successfully migrated into the Matrigel matrix (Supplementary Fig. 3). These results suggest that while infection does not suppress macrophage mesenchymal migration, parasite-enhanced migration primarily activates an integrin-independent and Rho/ROCK-dependent amoeboid migratory mode.

The ability of Rho inhibition to block migration of infected cells implies that *T. gondii* enhances motility by acting at or upstream of Rho. *T. gondii* secretes an array of effector proteins into host cells, several of which interfere with innate immunity[38,39]. None of these effectors are known to target the host cytoskeleton, and the *T. gondii* genome does not encode obvious analogs to Rho GEFs or GAPs (http://toxodb.org). However, we hypothesized that the secreted *T. gondii* protein kinases ROP17 and ROP18 which we

previously showed to phosphorylate immunity-related GTPases (IRGs)[40] might also interact with Rho GTPases, perhaps acting by targeting one of several previously identified phospho-activated Rho GEFs[41].

We infected RAW 264.7 macrophages with *Δrop5*, *Δrop17*, and *Δrop18* parasites and determined that only *ROP17* was required for enhanced penetration into and travel through collagen (Fig. 4c–d), with *Δrop5* and *Δrop18* parasites enhancing migration as effectively as wild-type parasites (Fig. 4c–d). No synergy with ROP18 was evident, as *Δrop17Δrop18* parasites blocked migration no more effectively than *Δrop17* parasites (Fig. 4c–d). ROP17 shows kinase activity *in vitro*[40], but the functional relevance of this kinase activity remains untested. The ROP17 catalytic triad is conserved and easily identifiable (Fig. 4e)[42]. We generated *Δrop17* parasites complemented with either a cMYC-tagged wild-type *ROP17* allele, or mutant alleles where disruption of single catalytic triad residues (K312A, D436A) should ablate kinase activity. ROP17^{WT}-cMYC, ROP17^{K312A}-cMYC, and ROP17^{D436A}-cMYC were all expressed at similar levels and accumulated as immature pro-proteins and a mature processed variant (Fig 4F). Complementation of *Δrop17* with *ROP17^{WT}-cMYC* restored collagen migration, while both catalytic triad mutants phenocopied *Δrop17* (Fig. 4g), demonstrating that ROP17 kinase activity is required for enhanced migration.

If ROP17 functions by activating Rho signaling, this could also lead to inhibition of Rac-dependent process such as endothelial adherence and transmigration via Rho-Rac crosstalk[43]. Accordingly, we tested if ROP17 is involved in parasite inhibition of monocyte adherence to our hCMEC/D3 model BBB. Parasites lacking *ROP17* inhibited the adherence of THP-1 monocytes, although the observed decrease was less dramatic than wild-type parasites (Fig. 4h). This result suggests that while ROP17 contributes to parasite inhibition of endothelial adherence, another effector is required for complete suppression, in contrast to the essential role of ROP17 in enhanced migration through collagen-rich 3-D substrates.

ROP17 ablation slows parasite dissemination and eliminates enhanced tissue migration of infected monocytes *in vivo*

We then asked if ROP17-dependent enhancement of monocyte tissue migration alters parasite dissemination in the murine model. We used intravital bioluminescence imaging to observe parasite dissemination after challenge with luciferase-expressing parasites. In mice infected subcutaneously with knockout (*Δrop17::cLUC*) *vs*. complemented (*Δrop17::cLUC/ROP17-cMYC*) parasites, we found that ROP17-deficient parasites expanded at the injection site at a slight disadvantage and spread more slowly, resulting in lower parasite burdens in and outside of the infection nidus (Fig. 5a–c). Although partial, this reduced dissemination led to a significant enhancement in mouse survival (Fig. 5d).

Prior studies have theorized roles for ROP17 in promoting optimal *in vitro* growth in type II *T. gondii*[44], and in synergizing with ROP18 in defending the parasitophorous vacuole from IFNγ-activated host IRGs[40]. We accordingly asked whether the delayed *in vivo* dissemination of our type I *Δrop17::cLUC* parasites could derive from deficiencies in intrinsic growth or resistance to IRG-mediated macrophage clearance. To test for inefficient parasite growth *in vivo*, we challenged mice intraperitoneally with *T. gondii*. Intraperitoneal infection challenges parasites with a robust immune response, while passive dissemination

via drainage from the peritoneal cavity likely negates motility differences. Hence, intraperitoneal infection should reveal mutants with specific defects in intrinsic growth or enhanced clearance susceptibility. After intraperitoneal challenge, we observed no difference in the virulence of knockout and complemented *Δrop17::cLUC* parasites (Fig. 5e). Likewise, *in vitro* assays established that *Δrop17::cLUC* parasites did not exhibit significant differences in mean plaque number or size when propagated in fibroblasts and compared to complemented *Δrop17::cLUC/ROP17-cMYC* parasites, and formed parasitophorous vacuoles of normal morphology and quantity when parasites were grown in IFNγ/LPS-activated RAW 264.7 murine macrophages (Supplementary Fig. 4). These findings suggest that the *in vivo* attenuation of *Δrop17::cLUC* parasites is specifically caused by deficient dissemination.

Finally, we used two-photon imaging to assess if ROP17 was critical for parasites to enhance monocyte tissue migration *in vivo*. We focused on the spleen as it is readily infected during natural *T. gondii* infections[11] and is the major tissue reservoir of murine monocytes[45]. We first tested whether we could detect monocytes by intravital two-photon spleen imaging in CX3CR1$^{gfp/+}$ mice, in which the vast majority of splenic CX3CR1+ cells are monocytes or lineage descendants[45]. We differentiated CX3CR1$^{gfp/+}$ monocytes and phagocytes by morphology, and successfully identified uninfected and infected CX3CR1$^{gfp/+}$ cells exhibiting monocyte morphology and staining with the monocyte marker CD115 (Supplementary Fig. 5). This staining pattern is consistent with identity as monocytes or still differentiating monocyte-derived phagocytes. We next found that wild-type *T. gondii* infection significantly increased the migration of splenic CX3CR1$^{GFP/+}$ cells with monocyte morphology, enhancing median track speed, mean square displacement, and median track straightness (Fig. 6a–c, left). In contrast, *Δrop17* infection had no statistically significant effect on measured motility parameters (Fig. 6a–c, right). Consistent with our observations of motility in the BBB model (Fig. 2), infected CX3CR1$^{GFP/+}$ cells migrated *in vivo* with a flowing amoeboid morphology suggestive of integrin-independent interstitial migration (Fig 6d–f, Videos 5–6). Next, we used an *ex vivo* spleen explant model (Fig. 6g–h) to test whether the enhanced migration of CX3CR1$^{GFP/+}$ cells with monocyte morphology was sensitive to ROCK inhibition, as expected for amoeboid interstitial migration. Treatment with Y-27632 significantly inhibited migration, decreasing median track speed and mean square displacement of infected CX3CR1$^{GFP/+}$ cells (Fig. 6i–l). Overall, our intravital and *ex vivo* imaging data strongly support the model that ROP17-dependent enhancement of amoeboid interstitial migration in infected monocytes promotes parasite dissemination through tissues *in vivo*.

DISCUSSION

Like several other pathogens, *T. gondii* is proposed to exploit leukocytes as Trojan horses that enable access to the CNS[2]. However, evidence for dissemination of *T. gondii* infected monocytes across the BBB currently lacks compelling supporting data. Here we show that *in vitro*, *T. gondii* infection profoundly impaired monocyte transmigration across a model BBB and integrin-dependent adherence to endothelium. In contrast, infection enhanced monocyte and macrophage motility on endothelial cells and interstitial migration through 3-D tissues, both *in vitro* and *in vivo*. Enhanced tissue migration was sensitive to pharmacological

inhibition of Rho/ROCK as is typical of integrin-independent amoeboid interstitial migration. We further identified the secreted parasite kinase ROP17 as essential for *T. gondii* to activate tissue migration. By infecting mice with ROP17-deficient *T. gondii*, we showed that loss of parasite-enhanced monocyte/macrophage tissue migration leads to slower parasite dissemination kinetics and prolonged mouse survival. In summary, we show that *T. gondii* dissemination is promoted by ROP17-dependent activation of interstitial tissue migration in infected monocytes, while integrin-dependent processes that lead to endothelial traversal are suppressed.

Although integrins were once thought to be pivotal players for all leukocyte migratory modes, elegant genetic work in mice has established that integrin-independent migration is possible within tissues[26]. When leukocytes interact with vasculature, integrins function as adhesins that enable stable adherence to endothelial ligands and as critical force-transducers that convert retrograde actin polymerization into forward movement[46]. However, the 3-D environments of tissue interstitial space de-emphasize the importance of adhesion. In such tissue environments, low affinity interactions with the surrounding matrix and Rho/ROCK-driven actin-based contractility can propel leukocytes forward, even in the absence of integrin functionality [26,46]. Here we report that *T. gondii* infection of monocytes simultaneously inhibited integrin-dependent processes and activates Rho-dependent tissue motility. The failure of infected monocytes to efficiently perform integrin-mediated adherence or TEM suggests that they are ill-suited to act as Trojan horses that deliver parasites across the BBB. Instead, we speculate that enhanced tissue migration could carry infected monocytes via lymphatic drainage into the circulation, by enhancing rates of either leukocyte entry into lymphatics or travel through lymph nodes and subsequent exit into efferent lymphatics that lead towards the lymphovenous valve. Once in the circulation, parasites may egress from infected monocytes and directly invade brain endothelium[9], a process that could perhaps be aided by infected monocytes embolizing in small CNS capillaries.

Our studies demonstrate that *T. gondii* infection programs monocytes to preferentially migrate through tissues in an amoeboid manner by using the secreted kinase ROP17 to activate Rho/ROCK-dependent processes. During natural infections, *T. gondii* first encounters and infects leukocytes in the intestinal lamina propria[6]. We speculate that *T. gondii* invades lamina propria monocytes or monocyte-derived macrophages early during infection and activates their tissue migration in order to rapidly escape this compartment. We focused on monocyte and macrophage motility due to the abundance of infected monocytes in the blood during murine infections[11]. Additionally, *T. gondii* manipulates DC motility[17–20], and DCs are infected in the lamina propria, although again less commonly than monocytes and macrophages[6]. The specific leukocyte subsets that are the primary target(s) of ROP17-mediated enhanced tissue migration *in vivo* remains a question for further study. Consistent with a role in dissemination, we showed that infection enhanced *in vivo* migration of $CX3CR1^{+}$ monocytes in the spleen, and that loss of ROP17-dependent enhanced tissue migration delayed the dissemination of hypervirulent type I *T. gondii*. Similarly, *ROP17* ablation was reported to cause a near complete loss of brain cyst formation in cyst-competent type II *T. gondii*[44], likely as a consequence of reduced dissemination.

Our findings establish that catalytic activity of the secreted serine/threonine kinase ROP17 is required for *T. gondii* to enhance macrophage tissue migration. Prior work theorized that ROP17 forms a complex with the kinase ROP18 and regulatory pseudokinase ROP5, and synergizes with these partners to ensure parasite survival within activated macrophages by phosphorylating IRGs[40]. In contrast to this IRG defense system, we found that when enhancing tissue migration, ROP17 functions independently of ROP5 and ROP18. We presume that ROP17 enhances tissue migration by phosphorylating an unknown, non-IRG target, which might directly or indirectly regulate host Rho/ROCK signaling. ROP17 could access cytosolic substrates either when injected into the host cytosol during parasite invasion or following subsequent recruitment to the cytosolic face of the parasitophorous vacuole membrane[40,47]. We previously showed that ROP17 exhibits a strong preference for threonine phosphorylation and slight preference for surrounding hydrophobic residues[40]. Although kinase targets cannot be easily predicted from substrate preference motifs, Rho GEFs VAV and GEF-H1, Rho GAP DLC1, and Rho GDI1 can all be phosphoregulated[41], and are thus candidate substrates through which ROP17 could activate Rho-driven amoeboid migration. Alternatively, ROP17 may facilitate export of a separate effector, given the recent report that it facilitates translocation of dense granule proteins across the parasitophorous vacuole membrane [48]. Future elucidation of ROP17 substrates may provide exciting insights into *T. gondii* dissemination and the currently completely unknown mechanisms that prompt leukocytes to adopt integrin-independent migratory strategies *in vivo*.

MATERIALS AND METHODS

Parasite culture

T. gondii parasites were propagated in human foreskin fibroblasts (HFF) obtained from the laboratory of John Boothroyd at Stanford University. Type II ME49 mCherry parasites were used throughout Figures 1–3 unless otherwise indicated. All studies with ROP17 were performed in a Type I RH *Δku80 Δhxpgrt* background. Source and generation details for all *T. gondii* strains used are described in Supplementary Table 1.

Primary Human Monocytes

Primary human monocytes were obtained by flushing human peripheral blood from leukoreduction (LRS) chambers provided by the Washington University School of Medicine apheresis center, and then isolating monocytes via negative immunodensity selection with a RosetteSep Human Monocyte Enrichment Cocktail (Stem Cell Tech) and Ficoll-Paque sedimentation. To confirm successful isolation of monocytes, cells were analyzed for CD33 and CD14 positivity by flow cytometry. Monocytes were cryopreserved immediately after harvest in 7.5% DMSO and 10% human serum. Upon thaw, primary monocytes were cultured in RPMI supplemented with 10% human serum, 1% non-essential amino acids, 10 mM HEPES, and 100U/mL penicillin-1 μg/mL streptomycin.

Culture of cell lines

The human brain endothelial cell line hCMEC/D3[49] was obtained from the laboratory of Robyn Klein at Washington University and grown as previously described[21] from passages 28 to 34. THP-1 monocytes were cultured in RPMI media supplemented with 10% FBS.

RAW 264.7 macrophages were cultured in DMEM media supplemented with 10% FBS. All lines were confirmed as mycoplasma-negative with the e-Myco plus mycoplasma PCR detection kit (Boca Scientific) upon acquisition.

Culture of primary cells

Primary human aortic endothelial cells (HAEC) at passage 3 were obtained from Lonza and cultured in fully-supplemented EGM-2 media (Lonza). HAEC from passages five to seven were used in experiments. Primary human astrocytes were acquired from ScienCell and cultured in Astrocyte Media (ScienCell) in flasks coated with 2 μg/cm^2 collagen. Upon receipt, astrocytes were cryopreserved at passage 1. Thawed aliquots at passage 3 or 4 were used for experiments.

Growth of hCMEC/D3 on polyacrylamide pads

To provide a soft substrate for cell growth, 0.4% polyacrylamide pads were prepared in glass-bottom dishes as previously described[23], and then coated with 150 μg/mL rat collagen I. Dishes were each seeded with 5×10^4 hCMEC/D3 and grown until confluence. HUVEC EA.hy926 cells were obtained from ATCC and cultured in DMEM supplemented with 10% FBS.

Microscopy

In vitro imaging studies were performed on a Axio Observer Z1 inverted microscope (Zeiss) that features modules for conventional fluorescence, spinning disk confocal, and total internal reflection fluoresecence (TIRF) microscopy. Conventional fluorescence images were acquired with illumination from a Colibri LED light source (Zeiss) and ORCA-ER digital camera (Hammamatsu Photonics, Japan). Spinning disk and TIRF images were acquired using illumination from 488 nm and 561 nm solid state lasers (Zeiss) and Evolve 512 Delta EMCCD cameras (Photometrics). For all modules, Zen software (Zeiss) was used for image acquisition.

Time-lapse imaging of monocyte crawling on hCMEC/D3 endothelium

To quantify crawling, THP-1 monocytes were labeled with CellTrace Oregon Green 488 Carboxy-DFFDA (ThermoFisher), resuspended in Migration RPMI [phenol-red free RPMI supplemented with 3% FBS, 1% non-essential amino acids (Gibco), and 10 mM HEPES] and then infected with freshly-harvested *T. gondii* at an MOI of ~ 4.5 for 3–6 h. Just prior to imaging, the hCMEC/D3 dishes were changed to Migration RPMI and then equilibrated for ten min at 37°C in the incubation chamber of an inverted microscope. Alternating conventional bright-field and fluorescent images were captured at 1 min intervals over a 45-min period, using the above-described spinning disk microscopy system with a 40x C-Apochromat water immersion objective (N.A. 1.20). Automated tracking of individual monocytes' centroids was performed using *Volocity* software (PerkinElmer). To follow actin polymerization dynamics, cells were transfected with F-Tractin-eGFP one day prior to imaging crawling on soft substrate-supported hCMEC/D3. Actin polymerization videos were collected with the above spinning disc imaging system, using five-sec intervals over 5-min periods. Structures consistent with pseudopodia or blebs were manually counted.

Animals

All protocols requiring animals were approved by the Institutional Animal Care and Use Committee at the Washington University in St Louis School of Medicine. Mice were housed in Association for Assessment and Accreditation of Laboratory Animal Care International-approved facilities at Washington University. CX3CR1$^{GFP/+}$ mice were obtained from Jackson Laboratory or as generous gifts from Gwen Randolph (Washington University). CD1 mice were purchased from Charles River Lab.

Intravital two-photon imaging

Heterozygous CX3CR1$^{GFP/+}$ mice were infected with 2–4×10^7 Cell Tracker Red CMPTX-labeled *T. gondii* via tail vein injection. To label CD115, 40 μg PE-conjugated anti-CD115 was introduced retro-orbitally about 30 min prior to imaging. Time-lapse imaging was performed with a custom built 2P microscope[50,51] equipped with a Chameleon Vision II Ti:Sapphire laser (Coherent) and a 1.0 NA 20x water dipping objective (Olympus). SlideBook software (Intelligent Imaging Solutions) was used to control laser scanning, image acquisition and z-step movements. *In vivo* imaging of the spleen used a custom imaging chamber built in house[50]. Mice were anesthetized with 1.5% isoflurane in carbogen carrier gas and body temperature was maintained with a warming plate. The skin was cut away over the spleen and a small incision made in the peritoneal membrane to access the spleen. The spleen was lifted gently with forceps and a small portion secured to thin plastic support with VetBond adhesive. The upper chamber plate was lowered on to the tissue until contact was made with the coverslip and then the upper chamber filled with water for imaging. The plastic support was then clipped to the upper chamber plate with a hair pin to dampen movement artifacts. Small electrical heaters (resisters) attached to both the upper and lower chamber plates were used to prevent the mouse from becoming hypothermic. After the imaging preparation was completed and prior to imaging, the spleen was examined under the microscope to confirm that blood flow was robust in sinuses and blood vessels. CX3CR1-GFP cell migration was analyzed using 3D time-lapse imaging for up to 30min. Florescence was excited at 980nm and fluorescence emission detected by PMTs simultaneously using 495nm and 560nm dichroic filters: Blue (<495nm, SHG collagen), green (495–560nm, eGFP) and red (>560nm, CMTPX-Toxo). Auto fluorescence appears as mix of color (495–600nm) and thus can be discriminated from eGFP, and CMTPX. For time-lapse imaging, we acquired a 500×500×60μm volume as 31 sequential 2 μm z-steps with a time resolution of approximately 25s per time point and a X,Y resolution of 0.585 μm /pixel. Intravital imaging focused on the red pulp at <100 μm below the surface. Multi-dimensional data sets were exported as TIFFs and rendered in 3D using Imaris (Bitplane). Cell tracking and data analysis were performed using Imaris (Bitplane) and Motility Lab (2ptrack.net). CX3CR1+ cells were identified by GFP signal and tracked in 3-D with an automated Imaris protocol. Macrophages were manually excluded on the basis of morphology, and infected monocytes manually identified by signal from the Cell Tracker Red dye. To assess track speed and mean square displacement, infected monocytes were compared to all unambiguously uninfected monocytes with verified accurate tracks from the same videos (RH-infected, N=34; *Δrop17*-infected, N=42; uninfected, N>1000). Straightness was assessed in only subsets of each population chosen to have similar track

durations (RH-infected monocytes, 74%, RH-uninfected monocytes-42%, *Δrop17*-infected monocytes-95%, *Δrop17*-uninfected monocytes-66%).

Ex vivo two-photon imaging

For *ex vivo* imaging, spleens were harvested from CX3CR1$^{gfp/+}$ mice and adhered onto a plastic coverslip with VetBond adhesive. Spleens were sliced lengthwise with a microtome blade and incubated for 60 min with Cell Tracker Red CMPTX-labeled RH *Δku80 Δhx T. gondii* or buffer control. After gentle rinsing, the explanted spleen sections were then imaged with the above described two-photon imaging approach while being superfused with DMEM supplemented with either 30 μM Y27632 or equivalent volume DMSO and aerated with Carbogen gas (95% oxygen, 5% carbon dioxide). Image processing and analysis was as above.

In vivo infections and intravital luminescence imaging

8–10 week-old female CD1 mice were challenged intraperitoneally or subcutaneously in the right rear flank with 200 parasites. Luminescence imaging was performed on mice anesthetized with 2% isoflurane and injected intraperitoneally with D-luciferin (Biosynth AG) (150mg/kg) with a Xenogen IVIS200 machine. Luminescence data was analyzed with Xenogen Living Image software (Caliper Life Sciences). To quantify disseminated parasites, a region of interest of size fixed to the smallest area of parasite signal near the injection site was denoted as the infection focus, and the signal from this area subtracted from another fixed size region of interest that encompassed all parasite signal within each mouse.

Bone marrow-derived macrophages

Bone marrow-derived macrophages (BMDM) were harvested from the femurs of C57/BL6 mice with standard protocols, matured in BMDM Harvest Media (DMEM, 10% FBS, 5% horse serum, 40 μM L-glutamine, 100 μg/mL gentamicin, 20% L929-conditioned media), and maintained in BMDM Maintenance Media (DMEM, 10% FBS, 5% horse serum, 40 μM L-glutamine, 100 μg/mL gentamicin, 10% L929-conditioned media).

Generation of transgenic monocytes and macrophages

THP-1 monocytes were transfected using the Amaxa 4D Nucleofection system (Lonza) and cell line SG kit. For each transfection, 1 μg of plasmid DNA prepared with a PureLink HiPure Plasmid Midiprep Kit (Invitrogen) was used with 2×10^6 THP-1 monocytes. RAW 264.7 macrophages were transfected using Lipofectamine LTX with PLUS Reagent (Thermofisher) and 7 μg DNA per plasmid, prepared with a NucleoBond Xtra Midi EF kit (Macherey-Nagel). To generate a stable GFP-expressing line of RAW 264.7 macrophages, we introduced the plasmids pSB-100 and pSB-Bi-GP, followed by selection with 5 μg/mL puromycin and maintenance in 2.5 μg/mL puromycin [52].

Flow cytometry analysis of integrin expression and activation

THP-1 monocytes were infected with *T. gondii* at an MOI of ~4.5 for 3 h, or IC buffer in equivalent volume. Monocytes were then pelleted and resuspended in Integrin Activation Buffer (IAB) (Hanks's Balanced Salt Solution, 1 mM Ca^{2+}, 1 mM Mg^{2+}, 20 mM HEPES,

0.5% FBS pH 7.4) and equilibrated at 37°C for 60 min. To activate integrins, monocytes were treated with 9 mM $MnCl_2$ for 5 min at 37°C, then immediately transferred to ice. Live unpermeabilized cells were stained for integrin expression with primary monoclonal antibodies: activated LFA-1, mAb24 (Abcam); activated VLA-4, mAb 12G10 (Abcam); LFA-1, mAb TS2/4 (Biolegend); VLA-4, mAb 9F10 (Biolegend), and Alexa-488-conjugated anti-mouse-IgG secondary antibody for detection. After staining, cells were fixed with ice-cold 4% formaldehyde and stored at 4°C in PBS prior to analysis with a BD-FacsCanto. Forward and side scatter gating was used to separate monocytes from debris and extracellular parasites.

Parasite growth in activated macrophages

RAW 264.7 macrophages were activated for 18 h with mouse IFNγ (10 U/mL) and LPS (1 ng/mL), then infected with *T. gondii*. After 24 h, cells were fixed and parasites stained with anti-DG52 antibody. The number of parasitophorous vacuoles present in five fields per technical replicate was counted. RAW 264.7 macrophages were infected with *T. gondii*. After fixation and permeabilization with 0.05% saponin, cells were stained with anti-GRA7[53]

Static adherence of monocytes to hCMEC/D3

Optical grade black 96-well plates were seeded with 1×10^5 hCMEC/D3 cells per well and grown to confluence. The day prior to the adherence assay, hCMEC/D3 were activated overnight with IFNγ (200 U/mL) and TNFα (200 U/mL) as indicated. THP-1 monocytes were labeled with Cell Trace CFSE (Invitrogen), and then infected with *T. gondii* at an MOI of ~4.5. After four h of infection, 10×10^5 monocytes per well were transferred to the pre-activated hCMEC/D3 and allowed to adhere for 30 min at 37°C. Non-adherent monocytes were then removed by vigorous rinsing, and the remaining adherent monocytes were fixed with 4% formaldehyde. Samples were imaged with a Cytation 3 imager (Biotek), using automated cell finding from CFSE fluorescence to locate focal planes. Approximately 80% of the well bottom was imaged, and Gen5 software (Biotek) then used to quantify the number of adherent monocytes. Three independent experiments were performed; each with 5–6 technical replicates per condition.

Integrin staining and TIRF microscopy

THP-1 monocytes were pre-infected *T. gondii* for 4 h (MOI=4) and then allowed to adhere onto 50 μg/mL fibronectin-coated glass coverslip dishes (MatTek) for 30 min. Samples were then gently rinsed with PBS and fixed for 10 min with ice-cold 4% formaldehyde in PBS. Cells were permeabilized with 0.05% saponin and stained with monoclonal antibodies to LFA-1 (TS2/4) or VLA-4 (9F10), followed by Alexa fluorophore-conjugated secondary antibodies. Samples were imaged in PBS with the earlier-described TIRF microscopy system and a 100x oil Plan-Apochromat (N.A. 1.46) objective. Tandem Z-stack series of the same cells were captured with the earlier-described spinning disc system to visualize cells as infected or uninfected. TIRF images were analyzed in *Volocity* software. Cell outlines were manually traced, and integrin foci were identified using the *Volocity* Spot Finder function.

Transendothelial migration assays

Transendothelial migration (TEM) was quantified by allowing CFSE-labeled monocytes to cross *in vitro* barriers of endothelial cells grown on 24-well format Falcon transwell permeable supports with PET membranes and 8-μm pores. To create a flat surface for automated imaging, 15 mm coverslips coated with 0.1% gelatin were placed in the basal chambers. After allowing for transmigration, transwell inserts were removed and basal chambers were fixed with 0.4% formaldehyde. Rectangular grids covering about 90% of the basal chambers were then imaged in medium-throughput format using a Cytation 3 (Biotek) plate imager with 10x objective. Gen5 software (Biotek) was used to quantify the number of monocytes in each basal chamber, as defined by size and fluorescence signal. Where indicated, chemotactic gradients were generated by adding 100 ng/mL MCP-1 chemokine (Peprotech) to basal transwell chambers. The hCMEC/D3 cell line was seeded onto transwell membranes pre-coated with 150 μg/mL rat collagen I, using 4–5×10^5 cells/cm^2 and grown 5–7 days prior to TEM assays. Barrier integrity was confirmed by measuring TEER with an EVOM2 Voltohmmeter (World Precision Instruments). At the time of TEM assays, hCMEC/D3 cells typically achieved a TEER of 50–70 ohms/cm^2.

For assays using HAEC and HUVEC EA.hy926 cells were seeded 10 μg/mL fibronectin-coated transwell membranes using 0.5–1×10^5 cells/cm^2 and cultured for two days to generate a robust barrier. Barrier integrity was confirmed by measuring transendothelial electrical resistance (TEER) with an EVOM2 Voltohmmeter (World Precision Instruments). At the time of TEM assays, HAEC cells typically achieved a TEER pf 40–50 ohms/cm^2 and HUVEC a TEER of 80–120 ohms/cm^2.

Mesenchymal migration through matrigel

Matrigel (8.3mg/mL) was polymerized in optical-grade black 96-well plates for 45 min at 37°C and then equilibrated ≥ 60 min in DMEM supplemented with 3% serum. In each well, 1×10^5 BMDM pre-labeled with Cell Trace CFSE (Invitrogen) and pre-incubated with *T. gondii* (infection rate: ~75%) or buffer controls, and then were allowed to migrate into the matrix. After overnight migration at 37°C and 5% CO_2, the samples were rinsed with PBS and fixed with 4% formaldehyde. Z-stack image series of the BMDM captured within the collagen matrices were captured with the above-described spinning disk microscopy system and an EC Plan-Neofluar 10x (N.A. 0.30) objective. *Volocity* software was used to generate 3-D renderings of the Z-stacks and locate each macrophage using an automated Object Finding protocol based on fluorescence intensity and cell size. Vertical distance migrated was calculated as the distance between the centroid of the cell with the highest Z-position and every other cell. To ensure analyzed macrophages were not superficially adhered to the Matrigel surface or other macrophages, any cells with 25 micron of the Matrigel surface were excluded from analysis. The protease inhibitor cocktail (PIC) was prepared from the *Sigma* Protease Inhibitor Cocktail P1860 (aproptinin, bestatin, E-64, leupeptin, pepstatin A) supplemented with 5 μm GM 6001 (EMD Millipore).

Three-dimensional collagen migration assays

Collagen matrices were prepared from Nutragen Type I Bovine Collagen (Advanced BioMatrix) in 1X MEM Eagle supplemented with 7.5% sodium bicarbonate (pH 9) in

optical-grade black 96-well plates. Matrices were allowed to polymerize at 37°C for 60 min to overnight, and then equilibrated ≥ 60 min in monocyte growth media supplemented with 3% serum. In each well, 5×10^4 monocytes or macrophages pre-labeled with Cell Trace CFSE (Invitrogen) and pre-infected with *T. gondii* (THP-1: MOI 4.5 with ME49 mCherry, 4 h; RAW 264.7: MOI 3 with ME49 mCherry) were allowed to migrate into the matrix. After overnight migration at 37°C and 5% CO_2, the samples were rinsed with PBS and fixed with 4% formaldehyde. Z-stack image series of the monocytes captured within the collagen matrices were captured with the above-described spinning disk microscopy system and an EC Plan-Neofluar 10x (N.A. 0.30) objective. *Volocity* software was used to generate 3-D renderings of the Z-stacks and locate each monocyte using an automated Object Finding protocol based on fluorescence intensity and cell size. Vertical distance migrated was calculated as the distance between the centroid of the cell with the highest Z-position and every other cell.

Harvest of *ex vivo* dermal ear tissue and video microscopy of macrophage migration

Ventral ear sheets were harvested from 7–8 week old female BALB/C mice (Charles River Lab) and stained for laminin (Sigma Aldrich) with AlexaFluor555-conjugated secondary antibody as previously described[29]. GFP-expressing RAW macrophages were pre-infected for 3–5 h with ME49 mCherry parasites or IC buffer control, and then harvested by gentle scraping. Infected and uninfected macrophages were mixed together and given 20 min to crawl into the dorsal side of an ear sheet. Ear sheets were then rinsed and imaged dorsal side-down in a temperature (37°C) and CO_2 (5%)-controlled chamber and the inverted spinning disc microscope with a 20x EC Plan-Neofluar objective (N.A. 0.50). Videos were collected for 2 h at 3 min intervals, each with Z-stacks spanning 50–80 μm in 5-μm increments. *Zen* (Zeiss) software was used to correct drift with the Time Alignment function and deconvolve images with a regularized inverse filter and zero order g-difference [54]. A *Volocity* automated protocol was used to track all macrophages. Every macrophage track was manually examined to confirm track accuracy and infection status.

Statistical Analysis

Data-sets were analyzed in *Prism 7* (Graphpad). Normally distributed data were analyzed with one-way ANOVA and Holm-Sidak's multiple comparison's test. Non-normally distributed data were analyzed with Kruskal-Wallis Test and Dunn's multiple comparison's test. Whenever applicable, two-tailed *P*-values were calculated and corrected for multiple comparisons. Two-photon data was analyzed in Motility Lab (http://2ptrack.net/) using two-tailed Wilcoxon's tests to assess significance.

Supplementary Material

Refer to Web version on PubMed Central for supplementary material.

ACKNOWLEDGEMENTS

Thanks to John A Cooper for constructive comments, Robyn Klein and Tamara Doering for sharing hCMEC/D3 cells, Todd Fehniger for facilitating the acquisition of primary human monocytes, Felipe Santiago and Hamid Salimi for advice regarding the BBB model, Seonyoung Kim, Lihua Yang and the Washington University School of Medicine In vivo Imaging Core for technical support and fluorescent reporter mice for the intravital imaging

experiments and Gwen Randolph for generously sharing CX3CR1$^{GFP/+}$ mice. Work was supported in part by grants from the National Science Foundation to LLD (DGE-1143954), and National Institute of Health to MJM (R01AI077600), LDS (AI034036), and JAC (R35GM118171).

REFERENCES

1. Montoya JG & Liesenfeld O Toxoplasmosis. Lancet 363, 1965–76 (2004). [PubMed: 15194258]
2. Santiago-Tirado FH & Doering TL False friends: Phagocytes as Trojan horses in microbial brain infections. PLoS Pathog 13, e1006680 (2017). [PubMed: 29240825]
3. Harker KS, Ueno N & Lodoen MB Toxoplasma gondii dissemination: a parasite's journey through the infected host. Parasite immunology 37, 141–9 (2015). [PubMed: 25408224]
4. Dubey JP Bradyzoite-induced murine toxoplasmosis: stage conversion, pathogenesis, and tissue cyst formation in mice fed bradyzoites of different strains of Toxoplasma gondii. J Eukaryot Microbiol 44, 592–602 (1997). [PubMed: 9435131]
5. Dubey JP, Speer CA, Shen SK, Kwok OC & Blixt JA Oocyst-induced murine toxoplasmosis: life cycle, pathogenicity, and stage conversion in mice fed Toxoplasma gondii oocysts. J Parasitol 83, 870–82 (1997). [PubMed: 9379292]
6. Gregg B et al. Replication and distribution of Toxoplasma gondii in the small intestine after oral infection with tissue cysts. Infect Immun 81, 1635–43 (2013). [PubMed: 23460516]
7. Joeris T, Muller-Luda K, Agace WW & Mowat AM Diversity and functions of intestinal mononuclear phagocytes. Mucosal Immunol 10, 845–864 (2017). [PubMed: 28378807]
8. Dunay IR et al. Gr1(+) inflammatory monocytes are required for mucosal resistance to the pathogen Toxoplasma gondii. Immunity 29, 306–17 (2008). [PubMed: 18691912]
9. Konradt C et al. Endothelial cells are a replicative niche for entry of Toxoplasma gondii to the central nervous system. Nature Microbiology 1, 16001 (2016).
10. Ley K, Laudanna C, Cybulsky MI & Nourshargh S Getting to the site of inflammation: the leukocyte adhesion cascade updated. Nature reviews. Immunology 7, 678–89 (2007).
11. Courret N et al. CD11c- and CD11b-expressing mouse leukocytes transport single Toxoplasma gondii tachyzoites to the brain. Blood 107, 309–16 (2006). [PubMed: 16051744]
12. Ueno N et al. Real-time imaging of Toxoplasma-infected human monocytes under fluidic shear stress reveals rapid translocation of intracellular parasites across endothelial barriers. Cellular microbiology 16, 580–95 (2014). [PubMed: 24245749]
13. Lambert H, Dellacasa-Lindberg I & Barragan A Migratory responses of leukocytes infected with Toxoplasma gondii. Microbes and infection / Institut Pasteur 13, 96–102 (2011).
14. Ueno N & Lodoen MB From the blood to the brain: avenues of eukaryotic pathogen dissemination to the central nervous system. Current opinion in microbiology 26, 53–9 (2015). [PubMed: 26048316]
15. Cook JH, Ueno N & Lodoen MB Toxoplasma gondii disrupts beta1 integrin signaling and focal adhesion formation during monocyte hypermotility. J Biol Chem (2018).
16. Harker KS et al. Toxoplasma gondii modulates the dynamics of human monocyte adhesion to vascular endothelium under fluidic shear stress. Journal of leukocyte biology 93, 789–800 (2013). [PubMed: 23485448]
17. Olafsson EB, Varas-Godoy M & Barragan A Toxoplasma gondii infection shifts dendritic cells into an amoeboid rapid migration mode encompassing podosome dissolution, secretion of TIMP-1, and reduced proteolysis of extracellular matrix. Cell Microbiol 20(2018).
18. Lambert H, Vutova PP, Adams WC, Loré K & Barragan A The Toxoplasma gondii-shuttling function of dendritic cells is linked to the parasite genotype. Infection and immunity 77, 1679–88 (2009). [PubMed: 19204091]
19. Fuks JM et al. GABAergic signaling is linked to a hypermigratory phenotype in dendritic cells infected by Toxoplasma gondii. PLoS Pathog 8, e1003051 (2012). [PubMed: 23236276]
20. Weidner JM et al. Rapid cytoskeleton remodelling in dendritic cells following invasion by Toxoplasma gondii coincides with the onset of a hypermigratory phenotype. Cellular microbiology 15, 1735–52 (2013). [PubMed: 23534541]

21. Daniels BP et al. Immortalized human cerebral microvascular endothelial cells maintain the properties of primary cells in an in vitro model of immune migration across the blood brain barrier. Journal of neuroscience methods 212, 173–9 (2013). [PubMed: 23068604]
22. van Kooyk Y & Figdor CG Avidity regulation of integrins: the driving force in leukocyte adhesion. Current Opinion in Cell Biology 12, 542–547 (2000). [PubMed: 10978887]
23. Onken MD et al. Endothelial monolayers and transendothelial migration depend on mechanical properties of the substrate. Cytoskeleton (Hoboken, N.J.) 71, 695–706 (2014).
24. Belin BJ, Goins LM & Mullins RD Comparative analysis of tools for live cell imaging of actin network architecture. Bioarchitecture 4, 189–202 (2014). [PubMed: 26317264]
25. Charras G & Paluch E Blebs lead the way: how to migrate without lamellipodia. Nat Rev Mol Cell Biol 9, 730–6 (2008). [PubMed: 18628785]
26. Lammermann T et al. Rapid leukocyte migration by integrin-independent flowing and squeezing. Nature 453, 51–5 (2008). [PubMed: 18451854]
27. Kanatani S, Uhlen P & Barragan A Infection by Toxoplasma gondii Induces Amoeboid-Like Migration of Dendritic Cells in a Three-Dimensional Collagen Matrix. PLoS ONE 10, e0139104 (2015). [PubMed: 26406763]
28. Wolf K et al. Collagen-based cell migration models in vitro and in vivo. Seminars in cell & developmental biology 20, 931–41 (2009). [PubMed: 19682592]
29. Weber M & Sixt M Live cell imaging of chemotactic dendritic cell migration in explanted mouse ear preparations. Methods Mol Biol 1013, 215–26 (2013). [PubMed: 23625502]
30. Cougoule C et al. Blood leukocytes and macrophages of various phenotypes have distinct abilities to form podosomes and to migrate in 3D environments. European Journal of Cell Biology 91, 938–949 (2012). [PubMed: 22999511]
31. Van Goethem E, Poincloux R, Gauffre F, Maridonneau-Parini I & Le Cabec V Matrix Architecture Dictates Three-Dimensional Migration Modes of Human Macrophages: Differential Involvement of Proteases and Podosome-Like Structures. The Journal of Immunology 184, 1049–1061 (2010). [PubMed: 20018633]
32. Lämmermann T & Germain RN The multiple faces of leukocyte interstitial migration. Seminars in immunopathology 36, 227–51 (2014). [PubMed: 24573488]
33. Shang X et al. Rational design of small molecule inhibitors targeting RhoA subfamily Rho GTPases. Chem Biol 19, 699–710 (2012). [PubMed: 22726684]
34. Martiny-Baron G et al. Selective inhibition of protein kinase C isozymes by the indolocarbazole Go 6976. J Biol Chem 268, 9194–7 (1993). [PubMed: 8486620]
35. Rizvi SA et al. Identification and characterization of a small molecule inhibitor of formin-mediated actin assembly. Chem Biol 16, 1158–68 (2009). [PubMed: 19942139]
36. Nolen BJ et al. Characterization of two classes of small molecule inhibitors of Arp2/3 complex. Nature 460, 1031–4 (2009). [PubMed: 19648907]
37. Van Goethem E, Poincloux R, Gauffre F, Maridonneau-Parini I & Le Cabec V Matrix architecture dictates three-dimensional migration modes of human macrophages: differential involvement of proteases and podosome-like structures. Journal of immunology 184, 1049–61 (2010).
38. Hunter CA & Sibley LD Modulation of innate immunity by Toxoplasma gondii virulence effectors. Nature Reviews Microbiology 10, 766–778 (2012). [PubMed: 23070557]
39. Hakimi MA, Olias P & Sibley LD >Toxoplasma Effectors Targeting Host Signaling and Transcription. Clin Microbiol Rev 30, 615–645 (2017). [PubMed: 28404792]
40. Etheridge Ronald D. et al. The Toxoplasma Pseudokinase ROP5 Forms Complexes with ROP18 and ROP17 Kinases that Synergize to Control Acute Virulence in Mice. Cell Host & Microbe 15, 537–550 (2014). [PubMed: 24832449]
41. Hodge RG & Ridley AJ Regulating Rho GTPases and their regulators. Nature Reviews Molecular Cell Biology 17, 496–510 (2016). [PubMed: 27301673]
42. Talevich E & Kannan N Structural and evolutionary adaptation of rhoptry kinases and pseudokinases, a family of coccidian virulence factors. BMC evolutionary biology 13, 117 (2013). [PubMed: 23742205]

43. Guilluy C, Garcia-Mata R & Burridge K Rho protein crosstalk: another social network? Trends in cell biology 21, 718–26 (2011). [PubMed: 21924908]
44. Fox BA et al. The Toxoplasma gondii Rhoptry Kinome Is Essential for Chronic Infection. miBio 7, e00193–16 (2016).
45. Swirski FK et al. Identification of splenic reservoir monocytes and their deployment to inflammatory sites. Science 325, 612–6 (2009). [PubMed: 19644120]
46. Renkawitz J & Sixt M Mechanisms of force generation and force transmission during interstitial leukocyte migration. EMBO Rep 11, 744–50 (2010). [PubMed: 20865016]
47. Hakansson S, Charron AJ & Sibley LD Toxoplasma evacuoles: a two-step process of secretion and fusion forms the parasitophorous vacuole. The EMBO journal 20, 3132–44 (2001). [PubMed: 11406590]
48. Panas MW et al. Translocation of dense granule effectors across the parasitophorous vacuole membrane in Toxoplasma-infected cells requires the activity of ROP17, a rhoptry protien kinase. bioRxiv (2019).
49. Weksler BB et al. Blood-brain barrier-specific properties of a human adult brain endothelial cell line. FASEB journal : official publication of the Federation of American Societies for Experimental Biology 19, 1872–4 (2005). [PubMed: 16141364]
50. Kreisel D et al. In vivo two-photon imaging reveals monocyte-dependent neutrophil extravasation during pulmonary inflammation. Proceedings of the National Academy of Sciences of the United States of America 107, 18073–8 (2010). [PubMed: 20923880]
51. Zinselmeyer BH et al. Chapter 16. Two-photon microscopy and multidimensional analysis of cell dynamics. Methods in enzymology 461, 349–78 (2009). [PubMed: 19480927]
52. Kowarz E, Loscher D & Marschalek R Optimized Sleeping Beauty transposons rapidly generate stable transgenic cell lines. Biotechnol J 10, 647–53 (2015). [PubMed: 25650551]
53. Alaganan A, Fentress SJ, Tang K, Wang Q & Sibley LD Toxoplasma GRA7 effector increases turnover of immunity-related GTPases and contributes to acute virulence in the mouse. Proceedings of the National Academy of Sciences of the United States of America 111, 1126–31 (2014). [PubMed: 24390541]
54. Schaefer LH, Schuster D & Herz H Generalized approach for accelerated maximum likelihood based image restoration applied to three-dimensional fluorescence microscopy. Journal of microscopy 204, 99–107 (2001). [PubMed: 11737543]

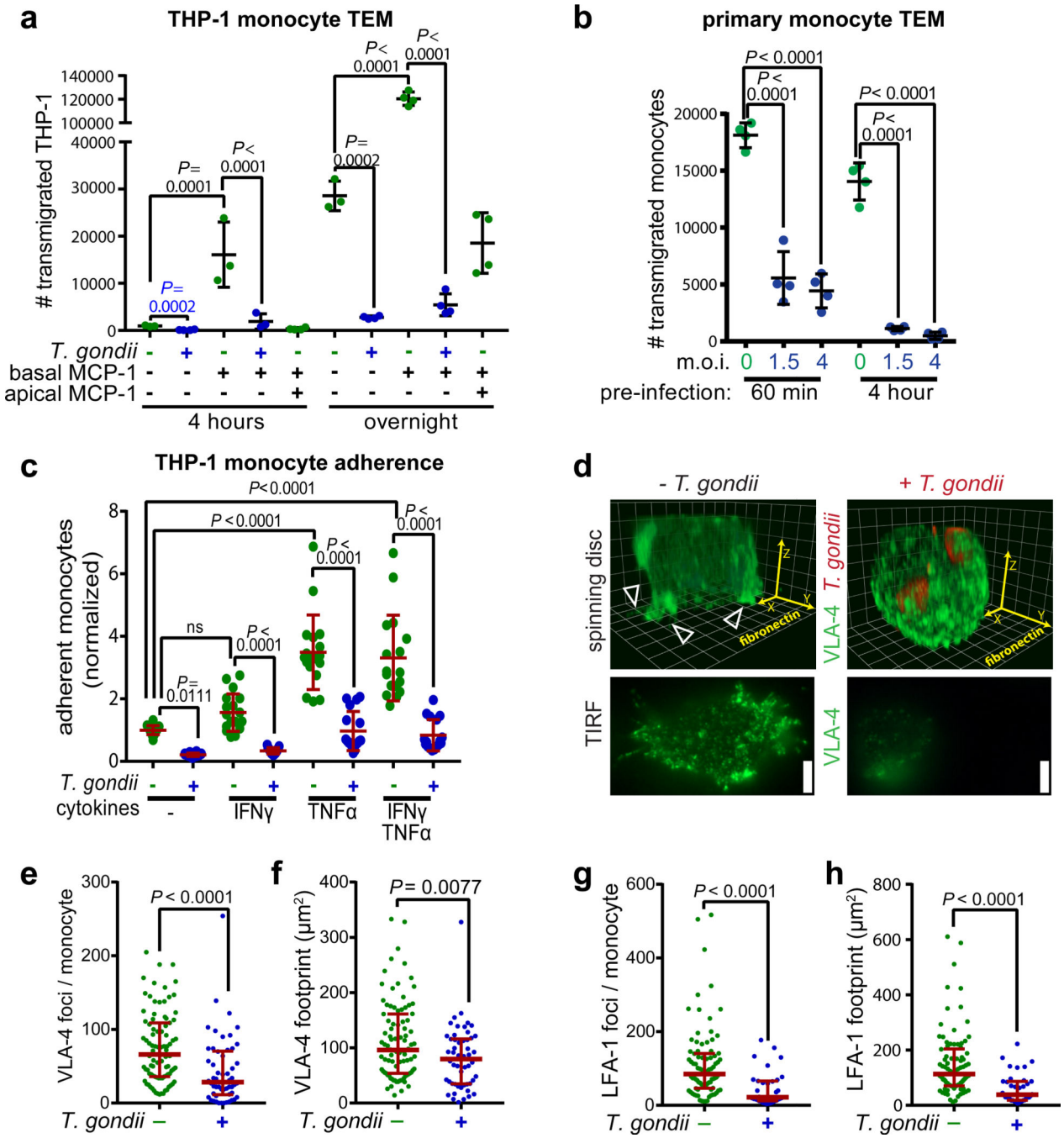

Fig. 1: Transendothelial migration and adherence of infected THP-1 and primary monocytes.

(a-b) Transmigration of THP-1 **(a)** and primary human monocytes **(b)** through a hCMEC/D3 BBB model, comparing infected cells (80–95% infected) to mock-treated controls. MCP-1 chemokine was added at 100 ng/mL as indicated. Prior to transmigration, monocytes were pre-infected with ME49-mCherry parasites. Data is shown from one experiment representative of two independent experiments with the same outcome. Each symbol indicates a within-experiment replicate biological sample (N=3–4/experiment). Lines and error bars denote mean ± SD. Multiplicity-adjusted *P*-values from one-way ANOVA and

Holm-Sidak's multiple comparison tests are shown in black (NS, $P > 0.05$); two-tailed P-values from unpaired t-tests are shown in blue. **(c)** Number of THP-1 monocytes adhered to hCMEC/D3 monolayers, comparing infected THP-1 (80–95% infected) to mock-treated controls. Data derived from three independent experiments, each with 5–6 within-experiment replicate biological samples. All quantities were normalized to the mean number of adhered uninfected cells. Error bars indicate mean ± SEM. Multiplicity-adjusted P-values from Holm-Sidak's multiple comparisons tests are shown (NS, $P > 0.05$). **(d-h)** THP-1 Monocytes adhering to fibronectin-coated glass were stained with antibodies to VLA-4 (mAb 9F10) and LFA-1 (mAb TS2/4). (**d**) Three-dimensional renderings from spinning disc confocal imaging (top) of VLA-4-stained mock- (left) and infected (right) THP-1 monocytes, and (bottom) sample TIRF microscopy images of the same cells. White arrowheads indicate spreading protrusions on the fibronectin surface. Scale bars = 5 μm. (**e-h**) Quantification of the number of integrin foci detected in TIRF images per THP-1 cell (**e,g**), and total integrin-contact-containing surface area occupied by individual cells in TIRF images (**f,h**). Each data point shows an individual monocyte (VLA-4 uninfected, N=89 THP-1 cells; VLA-4 infected, N=52 THP-1 cells; LFA-1 uninfected, N=85 THP-1 cells; LFA-1 infected, N=36 THP-1 cells). Lines indicate median and error bars interquartile ranges. Infected THP-1 cells were visually confirmed to contain intracellular parasites and compared to mock-treated control THP-1. Data were pooled from three independent experiments. Two-tailed P-values from unpaired Mann-Whitney tests are shown.

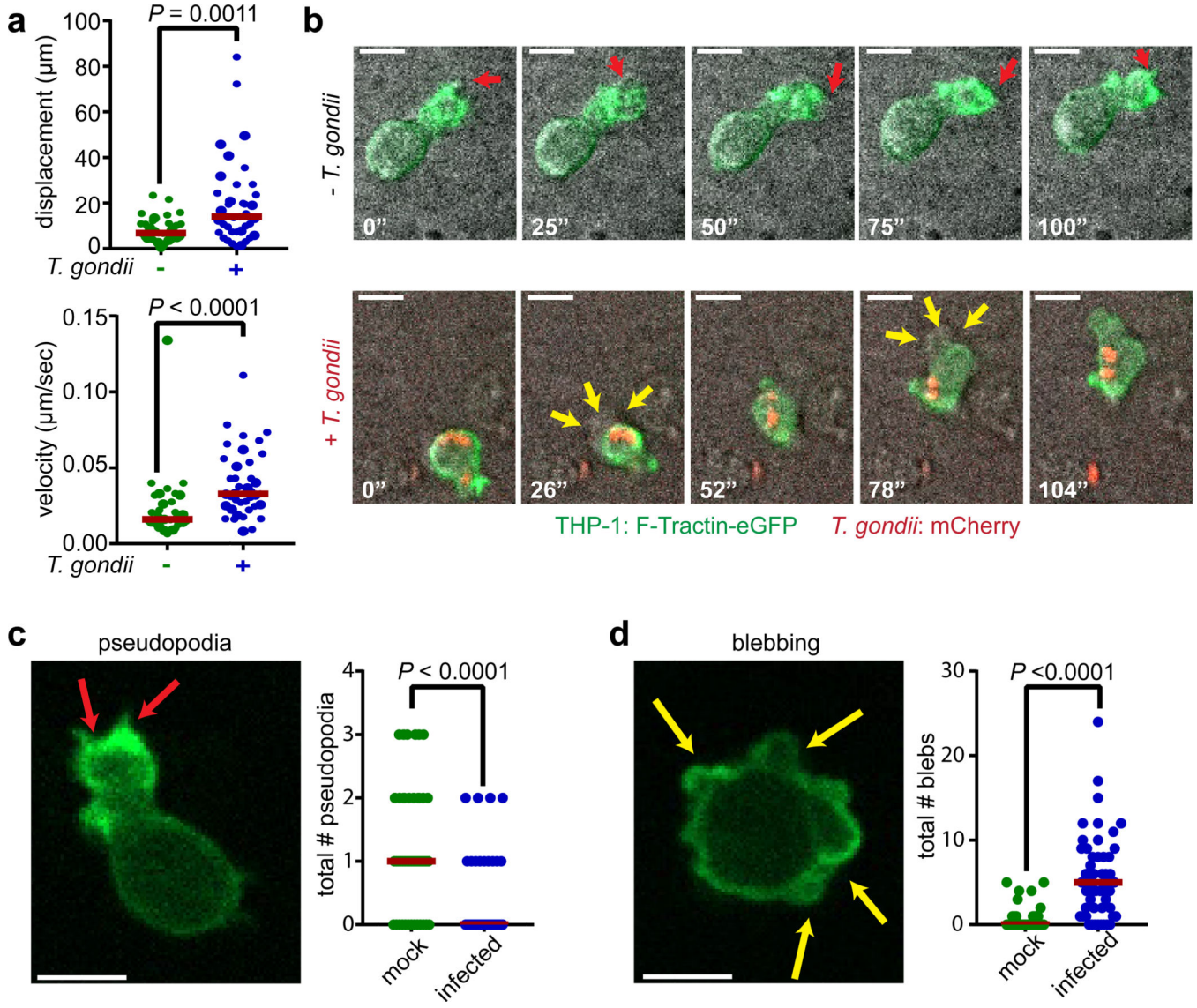

Fig. 2: Locomotion of infected THP-1 monocytes on hCMEC/D3 model of BBB.

(**a**) Displacement (top) and mean velocity (bottom) of THP-1 monocytes moving over hCMEC/D3 endothelial monolayers, as quantified from 45 min time-lapse microscopy videos. Data from three independent experiments were pooled (N= 8, 10, and 15 examples for mock-treated THP-1 monocytes; N= 12, 12, and 15 examples for infected), with manually confirmed infected THP-1 compared to mock-treated controls. (**b**) Time lapse images of crawling mock- (top) and *T. gondii*-infected (bottom) THP-1 monocytes expressing F-Tractin-eGFP. Red arrows indicate F-actin-rich pseudopodia. Yellow arrows indicate membrane swellings not enriched for F-actin. Images correspond to Supplementary Videos 1–2. (**c-d**) The number of structures consistent with pseudopodia **(c)** and blebs **(d)** formed by THP-1 monocytes during five min periods on hCMEC/D3 (mock, N=46 THP-1 cells; infected, N=51 THP-1 cells). Images show representative pseudopodia (red arrows) and blebs (yellow arrows) and correspond to Supplemental Videos 1 and 3. Data from three independent experiments were pooled. (**a-d**) Data points denote individual cells, and lines

median values. Two-tailed *P*-values from unpaired Mann Whitney tests are shown. All images show 10-μm scale bars and time in sec.

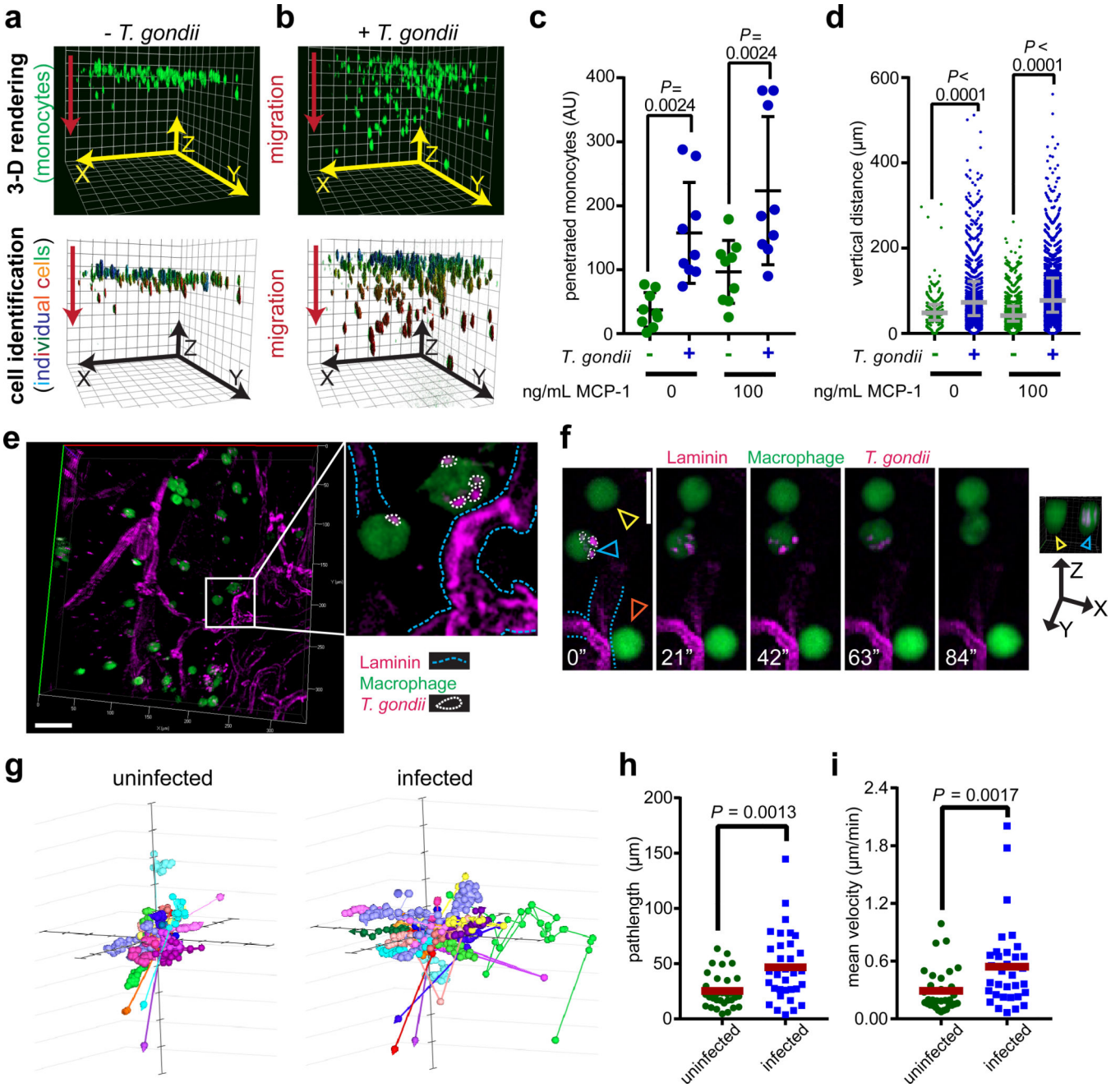

Fig. 3: Migration of infected cells through 3D collagen-matrices and skin tissue.

(a-b) Assay schematic, comparing mock-treated (a) and infected (b) THP-1 monocytes (infection rate: 80–95%). Top images show three-dimensional renderings created from spinning disk confocal images of THP-1 monocytes captured within collagen matrices. Red arrows indicate the direction of migration. Bottom images show individual cells located by automated protocol. **(c-d)** Number of penetrant cells (**c**) and vertical distance of each cell relative to the matrix top (**d**) was quantified after overnight migration. Plots show pooled data from three independent experiments, each with three technical replicates. **(e)** 3-D rendering of dermal ear sheet with vessels (magenta) stained for laminin. RAW macrophages

were visualized by GFP, and *T. gondii* by mCherry. Scale bar = 50 μm. Inset shows vessels traced in blue and intracellular parasites in white. **(f)** Time-lapse series showing a migrating infected cell, with ear dermis vessels traced in blue and intracellular parasites in white. Blue arrowhead indicates infected cell, yellow and orange arrowheads uninfected cells. Scale bar = 20 μm. Right inset shows a 3-D rendering cross-section demonstrating absence and presence of intracellular parasites in the cells. **(g)** Displacement plots of RAW macrophage trajectories through ear dermis tracked over a 2 h period, comparing uninfected and infected RAW macrophages manually identified from pools of ~50% infected cells. Total pathlength traveled (**h**) and average velocity (**i**) for each RAW cell in the displacement plots. Data was pooled from three independent experiments for a total N=33 of tracked RAW cells for both uninfected and infected. For all analyses, multiplicity-adjusted *P*-values are shown. Normally distributed data was analyzed with one-way ANOVA and Holm-Sidak's multiple comparison post-test and plotted as means ± SD **(c)**. Non-normally distributed data was analyzed with a Kruskal-Wallis test and Dunn's multiple comparison post-test and plotted with medians and interquartile ranges **(d,h-i)**.

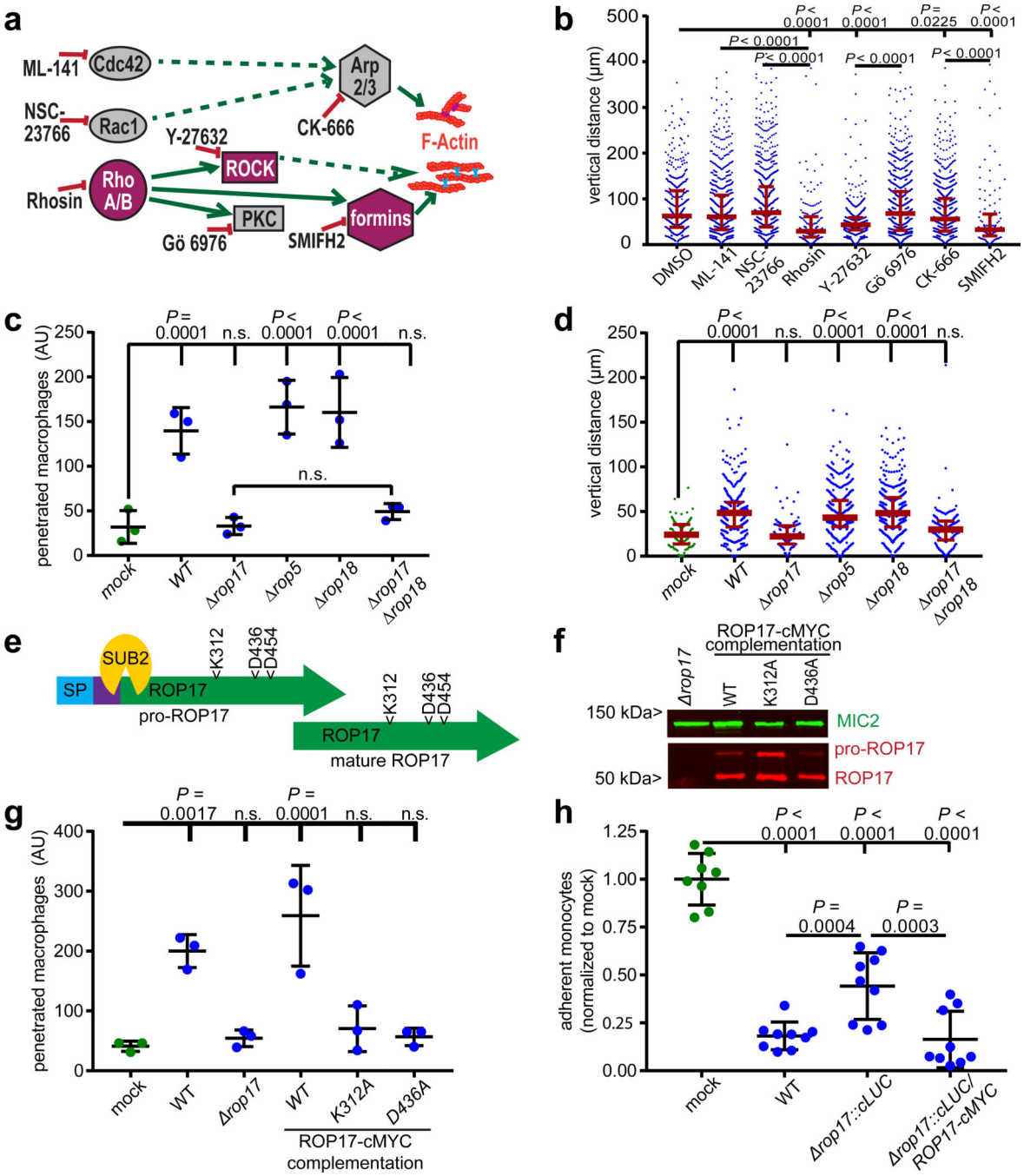

Fig 4: Enhanced tissue migration may involve Rho/ROCK and requires parasite ROP17.

(a) Rho GTPase signaling and inhibitors. **(b)** Distance migrated by infected THP-1 monocytes (infection rate: 80–95%, compared to mock-treated controls) into 0.8 mg/mL collagen I matrix loaded with 100 ng/mL MCP-1 chemokine, during inhibitor treatment (10 μM ML-141, 100 μM NSC-23766, 100 μM Rhosin, 30 μM Y-27632, 1 μM Gö 6976, 100 μM CK-666, 30 μM SMIFH2). **(c-d)** Migration of RAW 264.7 macrophages in 2 mg/mL collagen matrices after pre-infection with parasites of indicated genotype (infection rate ~90%, compared to mock-treated controls) (**c**- number penetrated cells, **d**- distance

traveled). **(e)** Schematic of ROP17 protein indicating catalytic triad residues and putative SUB2 processing site. **(f)** Western blot of samples from parasites of indicated genotype and probed with antibodies against cMYC and *T. gondii* MIC2. Blot is representative of two independent experiments.**(g)** Number of RAW macrophages migrated into a 2 mg/mL collagen matrix after pre-infection with *T. gondii* of indicated genotype (infection rate ~90%). **(h)** Adherence of THP-1 monocytes to IFNγ/TNFα- (200U/mL) stimulated hCMEC/D3 endothelial monolayers, comparing *T. gondii* pre-infection with indicated genotypes (infection rate 80–95%) to mock-treated controls. **(b-d, g)** Plots show data from one experiment representative of three independent assays, each with the same outcome and three replicate biological samples. **(h)** Pooled data from three independent assays is shown, each with three within-experiment biological replicate samples. Figures were normalized to the mean number of adherent mock-infected THP-1 monocytes in each experiment. **(b-d,g-h)**. Black lines and error bars indicate mean ± SD **(c,g,h)**, and red lines median and interquartile ranges **(b,d)**. Statistical significance was assessed with one-way ANOVA and Holm-Sidak's multiple comparison test for normally-distributed data (**c**, **g**, **h**), and Kruskal-Wallis test and Dunn's multiple comparisons test for non-normal distributions (**b**,**d**). For all analyses, multiplicity-adjusted *P* values are shown (n.s., $P > 0.05$).

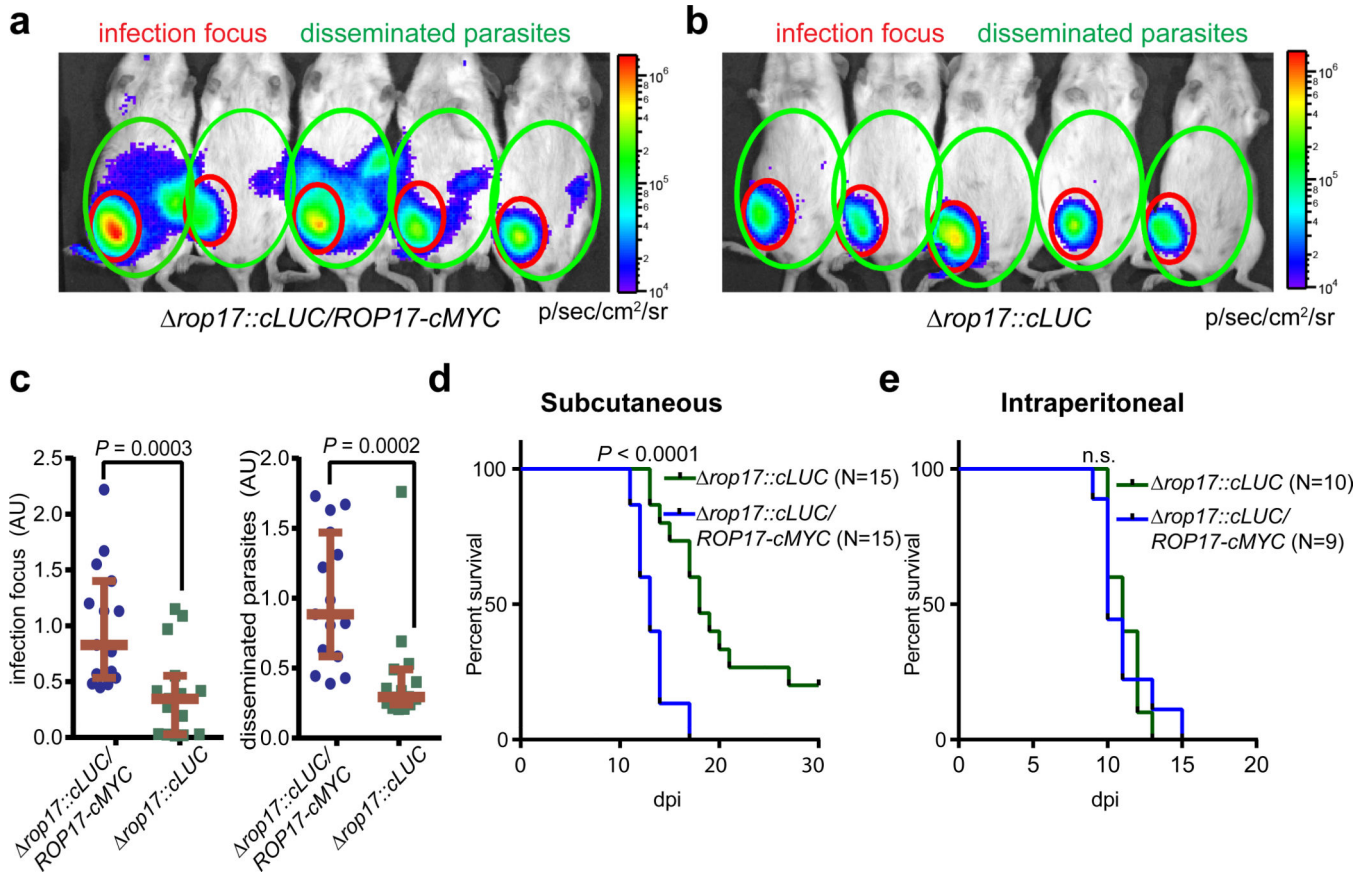

Fig 5: Role of ROP17 during *in vivo* infection.

Female CD1 mice were infected subcutaneously (**a-d**) or intraperitoneally (**e**) with 200 *T. gondii* of indicated genotype. Parasite burden and spread were monitored by intravital luminescence imaging prior to fatality (a-b, 8 days post-infection (dpi)), and survival monitored daily (**d,e**). Parasite luminescence signal in the infection focus was subtracted from total parasite signal in individual mice to quantify parasites disseminated beyond the infection nidus; representative images and quantification regions are shown (a-b). Pooled data from three independent subcutaneous infections (5 mice/group) and two independent intraperitoneal infections (4–5 mice/group) are shown as total normalized luminescence signal in individual mice (**c,** left: infection nidus; right: dissemination region) with median values and interquartile ranges indicated, and survival curves (**d,e**). Luminescence data was analyzed by two-tailed Mann-Whitney test, and mouse survival by a Gehan-Breslow-Wilcoxon test (n.s., $P > 0.05$, one tailed).

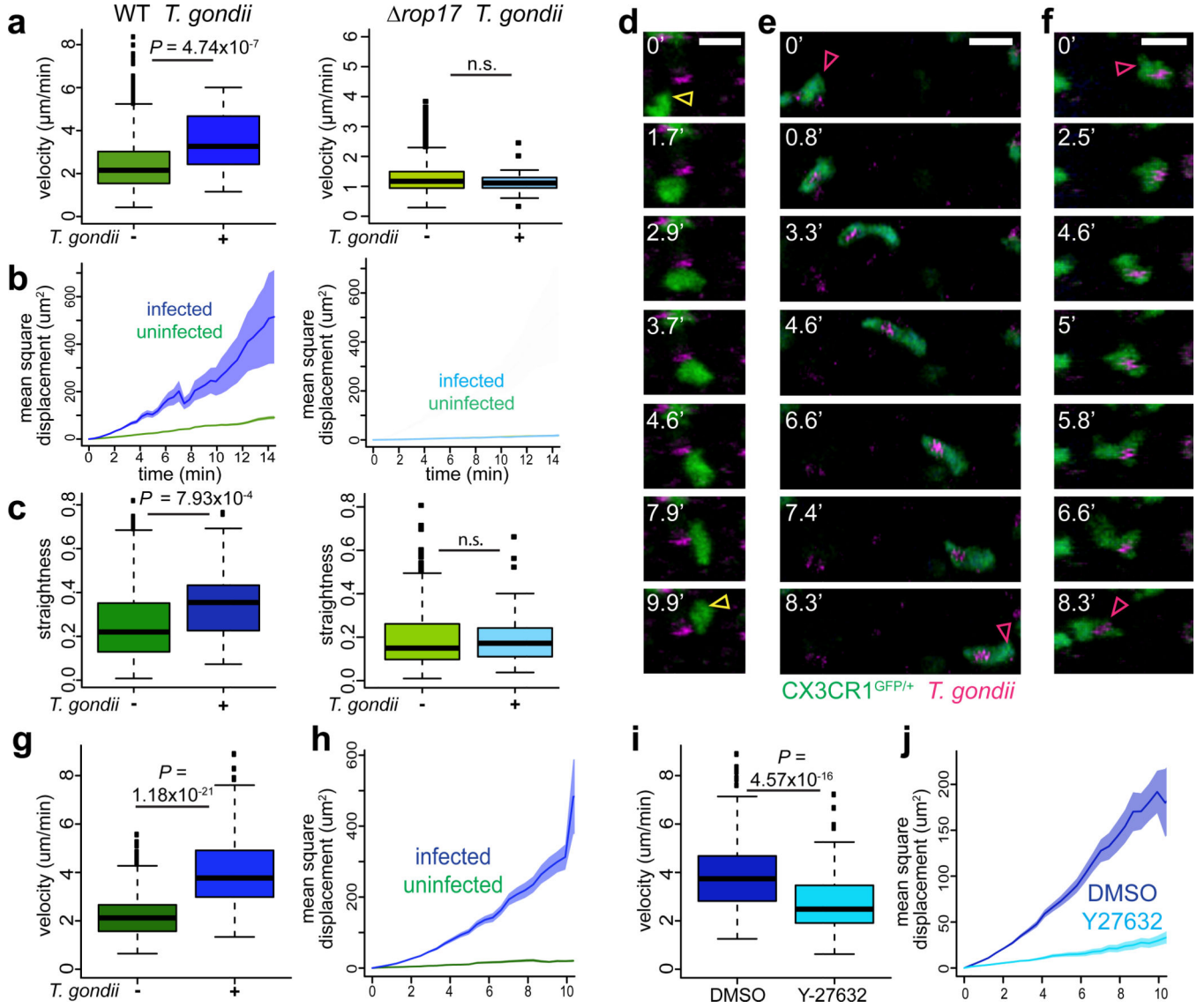

Fig. 6: *In vivo* and *ex vivo* motility of splenic CX3CR1$^{gfp/+}$ cells infected with wild-type and Δ*rop17* parasites.

(a-f) Intravital two-photon spleen imaging was performed 2–4 h after infecting CX3CR1$^{GFP/+}$ mice i.v. with 2–4×10^{7} wild-type or *Δrop17* parasites labeled with Cell Tracker Red CMPTX. **(a-c)** Track speed (**a**), mean square displacement (**b**) of all tracked cells, and median track straightness of the motile subset (**c**) is plotted, comparing infected and uninfected cells from the same videos (left: wild-type (WT) *T. gondii* infections, infected N=34, uninfected N=1783; right: *Δrop17* infections, infected N=42, uninfected N= 1228). **(d-f)** Time-lapse series of migrating cells displaying typical morphology. Start and end positions of migrating monocytes are indicated by yellow arrowheads (uninfected, **d**) and pink arrowheads (infected, **g-h**). Scale bars: 10 μm. Time shown in min. Images correspond to Supplementary Videos 4–6. **(g-j)** Two-photon imaging was performed after infecting *ex vivo* spleen sections for 60 min with wild-type Cell Tracker Red CMPTX-labeled *T. gondii* (tracked N=108), or buffer control (tracked N=148). **(i-j)** Spleen sections

were infected *ex vivo* and imaged during superfusion with 30 μM Y-27632 (tracked N=225) or equivalent volume DMSO (tracked N=175). Median track speed (**g,i**) and mean square displacement (**h,j**) of tracked CX3CR1$^{GFP/+}$ monocytes is plotted. Data was pooled from multiple videos captured during three **(a-c, i-j)** or one **(g-h)** independent experiment(s). Shaded areas indicate SEM for mean square displacement (**b,h,j**). In box-plots, medians and interquartile ranges are shown in colored bars, with min/max values indicated by black lines and outliers as dots for track speed (**a,g,i**) and straightness (**c**) plots. Data were analyzed by two-tailed Wilcoxon tests (n.s., $P > 0.05$).